The disordered and correlated insulator $Bi_2CrAl_3O_9$

J. C. Umana,[1] A. M. Baccarella,[1] L. Steinke,[2] A. Geritano,[1] Y. Janssen,[1] M. C. Aronson,[3] and J. W. Simonson[1,*]

[1]*Department of Physics, Farmingdale State College, Farmingdale, New York 11735, USA*

[2]*Department of Physics & Astronomy, Texas A&M University, College Station, Texas 77843, USA*

[3]*Stewart Blusson Quantum Matter Institute, University of British Columbia, Vancouver, British Columbia V6T 1Z4, Canada*

(Received 31 July 2019; published 19 September 2019)

The 3*d* transition metal insulator $Bi_2CrAl_3O_9$ forms with a quasi-one-dimensional structure characterized by linear chains of edge-sharing, Cr-and Al-centered, distorted octahedra. The UV/Vis spectrum of high-quality single crystals is marked by broad absorption edges corresponding to direct transitions across a 1.36-eV insulating gap. Measurements of dc magnetic susceptibility χ reveal a fluctuating moment of $2.60 \pm 0.01\ \mu_B$/Cr—reduced from the 3.87 μ_B/Cr expected for Cr^{3+}, while the Weiss temperature $\Theta_W = -21 \pm 1$ K implies that the prevailing local moment interactions are weakly antiferromagnetic in nature. Some 10% of the fluctuating moment is quenched, presumably due to the onset of an antiferromagnetic or spin glass phase at temperature $T^\star = 98 \pm 3$ K, while measurements of magnetization versus field H at $T \leqslant 10$ K scale as $H/T^{0.68(4)}$, suggesting the presence of quantum fluctuations associated with a disordered phase. Density functional theory calculations carried out within the generalized gradient approximation are in excellent agreement with experimental results, asserting that short-range magnetic interactions remnant above $T^\star$ stabilize the insulating state.

DOI: 10.1103/PhysRevB.100.104425

I. INTRODUCTION

$Bi_2M_4O_9$-type oxides, where M represents an ostensibly trivalent metal, form a class of narrow gap insulators that often host band edges or gap states with nearly dispersionless transition metal 3*d* character. Accordingly, these materials give rise to a wide variety of optical and magnetic phenomena, including photocatalysis [1], fluorescence [2–5], photocurrent excitations [6], magnetodielectric effects [7,8], and multiferroicity [9].

$Bi_2Fe_4O_9$ is a unique member of this class of materials in that it provides one of the few experimental realizations of the Cairo pentagonal lattice. Here, local magnetic moments situated at the vertices of a framework of nonregular pentagons form a geometrically frustrated, five-fold analogy to the threefold kagome lattice [10–12]. In general, Cairo pentagonal systems can be driven through several competing phase transitions by tuning the size of the moment and the ratios of the exchange coupling constants [12–14]. In the $J = 1/2$ quantum limit, strong quantum fluctuations may even give rise to exotic spin nematic and nonmagnetic phases [12,15]. For its part, $Bi_2Fe_4O_9$ is an antiferromagnet below Néel temperature $T_N = 264 \pm 3$ K with a large, $J = 5/2$ Fe^{3+} ordered moment reaching $4.95 \pm 0.08\ \mu_B$/Fe as $T \to 0$ K [16] and a correspondingly large fluctuating moment $6.3 \pm 0.3\ \mu_B$/Fe above T_N [10]. Upon ordering, the moments are constrained within the **ab** plane in a peculiar and frustrated magnetic structure consisting of two domains in which pairs of moments are oriented 90° from corresponding pairs on the same site in the opposite domain, realizing in the aggregate a fourfold rotational symmetry within an orthorhombic system [10].

Similar—if perhaps more complicated—physics arises in $Bi_4Fe_5O_{13}F$, which forms from a stacking variant of the $Bi_2Fe_4O_9$ Cairo pentagonal planes [17,18], providing a window into the inherent tunability of exchange interactions among the pentagonal elements. The crystal structures of these two intimately related compounds are composed predominantly of octahedra and tetrahedra of O arranged in layers within the **ab** plane, similar to the structure we show in Fig. 1. In both $Bi_2Fe_4O_9$ and $Bi_4Fe_5O_{13}F$, the octahedrally and tetrahedrally coordinated atomic positions are fully occupied by Fe^{3+} in the $3d^5$ configuration, and it is this network that gives rise to the Cairo pentagonal lattice within the plane.

We present in this work the crystal structure and the optical and magnetic properties of $Bi_2CrAl_3O_9$, an isostructural analog in which the magnetic species is relegated to a single, half-filled site. Unlike $Bi_2Fe_4O_9$, the tetrahedrally coordinated atomic positions of this analogous compound are occupied instead by nonmagnetic Al, while the octahedrally coordinated positions contain equal parts Al and $J = 3/2$ Cr^{3+}, distributed statistically. Because these octahedra are arranged in edge-sharing chains along **c**, $Bi_2CrAl_3O_9$ gives rise to a disordered, quasi-one-dimensional motif in place of the frustrated, quasi-two-dimensional Cairo lattice of $Bi_2Fe_4O_9$ and $Bi_4Fe_5O_{13}F$. Through optical and magnetic measurements on high-quality single crystal samples, we find in $Bi_2CrAl_3O_9$ a comparatively more itinerant system with a narrower band gap, a fluctuating moment markedly reduced from the Cr^{3+} free ion value, the onset of partial magnetic order at $T^\star = 98 \pm 3$ K, and the suggestion of quantum fluctuations emerging from this frustrated, disordered system as $T \to 0$ K.

*jack.simonson@farmingdale.edu

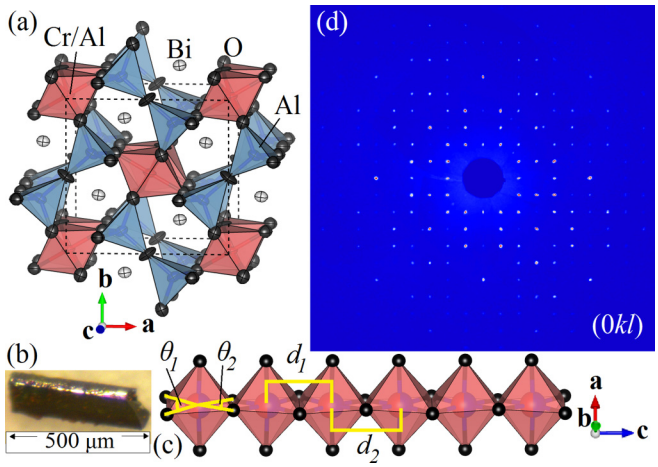

FIG. 1. (a) The unit cell of $Bi_2CrAl_3O_9$ with $Cr_{0.5}Al_{0.5}$-centered distorted octahedra colored in red, Al-centered tetrahedra colored in blue, Bi drawn in white, and O drawn in black, as indicated. The obtained space group is *Pbam*, and the lattice parameters are $a = 8.1354(12)$ Å, $b = 7.7532(10)$ Å, and $c = 5.7518(9)$ Å. Refinement parameters are residual $R = 2.58$, weighted residual $wR = 2.45$, and goodness of fit $S = 1.02$. (b) An optical microscope image of a typical crystal illustrating its plate-like habit. (c) A view of the chain of $Cr_{0.5}Al_{0.5}$-centered, distorted octahedra oriented along **c** with nearest-neighbor $(Cr_{0.5}Al_{0.5})$-$(Cr_{0.5}Al_{0.5})$ distances d_1 and d_2 and O-$(Cr_{0.5}Al_{0.5})$-O angles θ_1 and θ_2 indicated. Colors are as in (a). (d) The $(0kl)$ reciprocal space map showing well-indexed, clean, round reflections and no evidence of an occupancy-related superstructure.

II. METHODS

We grew single crystals of $Bi_2CrAl_3O_9$ as large as 500 μm × 100 μm × 50 μm from commercial Cr_2O_3 and Al_2O_3 powders and excess Bi_2O_3 flux. Some 2.5 g of these precursors were assembled in atomic ratios of 24 Cr_2O_3 + 5 Al_2O_3 + 76 Bi_2O_3, heated in air to 1323 K over a period of two hours, held at this temperature for two hours, and cooled to 1098 K over a period of 64 hours. After removal from the furnace, we mechanically extracted the green, translucent, platelike crystals from the regulus. We determined their crystal structure using an Oxford Gemini single-crystal diffractometer with Mo Kα radiation by employing a charge-flipping algorithm [19–21]. We collected UV-Vis diffuse reflectance spectra with photon wavelengths $\lambda = 900$ to 310 nm in a Cintra 40 double-beam spectrometer equipped with an integrating sphere and using $BaSO_4$ as a reference. The resolution in λ was 1.0 nm. We carried out dc magnetization measurements on a collection of single crystals enclosed within a gold sachet via a Quantum Design Physical Property Measurement System with the Vibrating Sample Magnetometer option. Samples were zero-field cooled to base temperature $T = 3$ K, a dc field was applied, and measurements were carried out upon warming. We performed density functional theory DFT calculations using the QUANTUM ESPRESSO package [22,23] with the Perdew-Burke-Ernzerhof parametrization of the exchange correlation potential in the generalized gradient approximation and with standard solid state pseudopotentials [24]. We found the onsite Coulomb interaction U and the intra-atomic Hund's exchange J_H from first principles by employing an internally consistent linear response technique [25,26].

III. RESULTS AND DISCUSSION

A. Quasi-one-dimensional, disordered crystal structure

As we show in Fig. 1(a), the crystal structure of $Bi_2CrAl_3O_9$ is composed of distorted, vertex-sharing octahedra and tetrahedra of O, while Bi occupy the interpolyhedral channels. Our refinement of single crystal x-ray diffraction data reveals that the tetrahedra are solely occupied by Al, while the octahedra are occupied by both Cr and Al. Our overall refined composition $Bi_2Cr_{1.01(2)}Al_{2.99(2)}O_9$ is indistinguishable from half Cr and half Al occupancy of the octahedral site. While we were able to synthesize crystals with lower Cr content, we were not able to increase the overall Cr:Al ratio beyond 1:3, suggesting an upper limit to Cr solubility in the $Bi_2Al_4O_9$ structure. Our results are in close agreement with those of previous reports of polycrystalline samples, in which Rietveld refinement of diffraction patterns from calcined powders resulted in $Bi_2Cr_xAl_{4-x}O_9$ with x no larger than 1.2 before the breakdown of Vegard's rule and the appearance of secondary phases [27]. On the other hand, our observation of transition metal site preference provides a marked contrast to $Bi_2Fe_xAl_{4-x}O_9$, in which Fe and Al atoms are distributed nearly uniformly across both sites [28]. Our x-ray diffraction refinement provides clear evidence that in $Bi_2CrAl_3O_9$, Cr is constrained to the octahedral site and the Cr:Al ratio on this site is 1:1 within a narrow window of experimental uncertainty. An example of our flux-grown single crystals is shown in Fig. 1(b).

Figure 1(c) offers a closer look at the distorted and disordered octahedrally coordinated $Cr_{0.50}Al_{0.50}$ sites in $Bi_2CrAl_3O_9$, which form edge-sharing chains along **c** with alternating nearest-neighbor distances between $Cr_{0.50}Al_{0.50}$ sites along the chain equal to $d_1 = 2.760(2)$ Å and $d_2 = 2.992(2)$ Å. For comparison, interchain $Cr_{0.50}Al_{0.50}$ distances are uniformly 5.6189(6) Å or longer, suggesting that magnetic interactions between nearest-neighbor Cr in this compound may be primarily quasi-one-dimensional. Meanwhile, intrachain O-$(Cr_{0.5}Al_{0.5})$-O angles $\theta_1 = 86.8(2)^\circ$ and $\theta_2 = 79.98(19)^\circ$, indicate significant distortion from the regular octahedron $\theta_1 = \theta_2 = 90^\circ$, indicating that energy levels associated with Cr^{3+} are likely to be additionally split by distortions from the ideal octahedral crystal field. Bond valence sums are 3.299(16) for the octahedrally coordinated Cr and 2.746(12) for the octahedrally coordinated Al, consistent with the expectation of Cr^{3+}. Meanwhile, the apparent modest underbonding of Al^{3+} and concurrent overbonding of Cr^{3+} suggests additional structural distortions of the octahedra that are not captured in the aggregate model. Specifically, local bond distances may be respectively on the order of 1% larger and smaller in the CrO_6 octahedra and AlO_6 octahedra than in the average model, contributing to composition-induced local strain within the octahedral chains.

It is conceivable in this structure that the Al and Cr occupying the distorted octahedrally coordinated sites could segregate in an orderly manner, thereby giving rise to a new

periodicity, perhaps most likely along the chain direction. On the contrary, Fig. 1(d) shows an example of a reciprocal space map of the $(0kl)$ plane, as integrated from our x-ray diffraction images, in which all spots are indexed by the lattice parameters. As shown in the figure, there is no evidence of any superstructure-derived reflections, such as might be related to occupancy ordering beyond the boundaries of the unit cell. Other reciprocal space planes are similarly well-indexed. The absence of any such reflections in the integrated maps indicates that if ordering occurs, it be limited to within the unit cell.

Accordingly, we also considered structural solutions with the maximal nonisomorphic, noncentrosymmetric space group *Pba*2 to address the possibility of reduced symmetry as would stem from ordered occupancy of the octahedrally coordinated site within the cell. This group lacks the inversion operator, the removal of which would permit Cr and Al to alternate freely within the octahedral chains. Even with this lower symmetry group, however, the residuals and the goodness-of-fit of our structure solutions are not improved over those associated with the *Pbam* space group of the $Bi_2Al_4O_9$ structure, suggesting that the Cr/Al occupancy of the octahedrally coordinated site likely remains disordered even at the unit cell level. We similarly considered monoclinic distortion of orthorhombic $Bi_2CrAl_3O_9$ to space groups $P2_1/c$ and $P2/c$ again without improving the quality of the refinement. This outcome suggests that the edge-sharing octahedra of Fig. 1(c) host a disordered, statistical distribution of N-member chains of Cr along c, where often $N = 1$, but also $N = 2, 3, 4, \ldots$ as populations of higher N chains arise with diminishing likelihoods.

B. Optical gap and Cr^{3+}-derived optical transitions

Figure 2 shows that $Bi_2CrAl_3O_9$ is an insulator with a narrow energy gap, the structure of which can be understood in terms of the local physics of octahedrally coordinated Cr^{3+}. In Fig. 2(a) we show the as-measured, background-subtracted diffuse reflectance spectrum collected from a mosaic of ~50-μm-thick single crystals mounted to the surface of an integrating sphere with light incident upon the (100) surfaces. Reflectance R approaches 100% at the low photon energy $h\nu$ end of the spectrum, demonstrating that the crystals approach transparency in the near infrared. R reaches a local minimum at 2.06 eV (602 nm) and a local maximum at 2.36 eV (525 nm), in excellent agreement with the observed green color of the crystals, before decreasing further as $h\nu$ increases, presumably due to photoexcitation of charge carriers across the gap. The dominant contribution to the spectrum consists of the two broad absorption bands indicated by dashed lines in the figure, which likely correspond to transitions of nearly octahedrally coordinated Cr^{3+} from the ground state to the first and second excited quartet states [29]. In terms of irreducible representations of the O_h group and of Cr $3d$ states, these two transitions equate to $^4A_2(t_2^3) \rightarrow ^4T_2(t_2^2e)$ and $^4A_2(t_2^3) \rightarrow ^4T_1(t_2^2e)$, respectively [30], and signify the promotion of a single electron from the O_h-stabilized t_{2g} states to an e_g state. The transitions are spin-allowed by Pauli exclusion, while their widths suggest

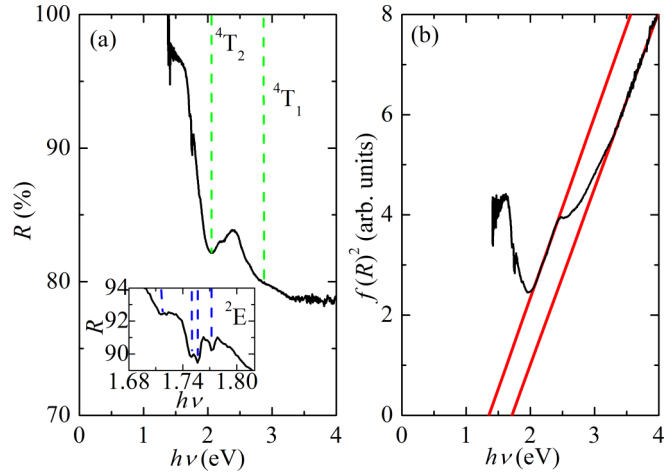

FIG. 2. (a) The UV-Vis diffuse reflectance R spectrum (black) of a mosaic of $Bi_2CrAl_3O_9$ single crystals plotted as a function of incident photon energy $h\nu$ from 1.38 to 4.00 eV, corresponding to wavelength $\lambda = 900$ to 310 nm. The green dashed lines are guides for the eye to indicate the positions of likely $^4A_2(t_2^3) \rightarrow ^4T_2(t_2^2e)$ and $^4A_2(t_2^3) \rightarrow ^4T_1(t_2^2e)$ transitions, as indicated. (Inset) The fine structure of the R lines, resulting from $^4A_2(t_2^3) \rightarrow ^2E(t_2^3)$ transitions. The dashed blue lines are guides for the eye. (b) The square of the Kubelka-Munk function $f(R)^2$ plotted vs $h\nu$ (black), where the solid red lines are best fits of the Tauc relation to the linear regions (see text).

substantial vibronic broadening associated with the emission of several phonons.

The sharp transitions shown more clearly in the inset to Fig. 2(a) are likely the so-called R lines, which signify lower energy transitions from the ground state to the excited doublet state $^4A_2(t_2^3) \rightarrow ^2E(t_2^3)$ involving no change of orbital. They are spin-forbidden but nevertheless occur due to spin-orbit coupling to spin-allowed bands within the same $h\nu$ range. We observe a fine structure consisting of four clear minima at 1.715, 1.749, 1.757, and 1.773 eV, suggesting that line splitting arises both from the distorted crystal field and from Cr^{3+} spin-orbit coupling ζ. The magnitudes of splitting we observe are consistent with typical values of ζ for Cr^{3+} in octahedral coordinations [29]. Additionally, we observe a small dip in R at 2.26 eV, which is a likely a Fano-type anti-resonance associated with a spin-forbidden $^4A_2(t_2^3) \rightarrow ^4T_2(t_2^3)$ transition [31]. As a whole, the spectrum reveals that $Bi_2CrAl_3O_9$ is an insulating system in which the Cr can be modeled as Cr^{3+} subject to spin orbit interactions as well as to a distorted octahedral crystal field that is consistent with our x-ray structural model. A key consequence of this model is its Cr^{3+} half-filled $^4A_2(t_2^3)$ ground state, which Hund's rules imply will yield magnetic moments with high-spin $J = 3/2$ configuration.

We estimate the energy gap of $Bi_2CrAl_3O_9$ from lines of best fit tangent to the square of the Kubelka-Munk function $f(R)^2$ as shown in Fig. 2(b). These tangent lines were determined from linear regression to the Tauc relation $\alpha h\nu = C(h\nu - E_g)^\beta$, for absorption coefficient α and band gap E_g, where C is a fitting parameter dependent in part upon the geometry of the exposed surface. The exponent β is dictated

by the nature of the allowed transitions across the gap, with $\beta = 1/2$ corresponding to direct transitions and $\beta = 2$ indirect. In the case of $Bi_2CrAl_3O_9$, the linear best fits are clearly superior when $\beta = 1/2$, suggesting that the gap is direct, as is that of $Bi_2Al_4O_9$ itself, which explicitly lacks $3d$ transition metal states near the gap [32].

The observed maximum in R at 2.36 eV [Fig. 2(a)] separates two distinct linear regions in $f(R)^2$, which intercept the $h\nu$ axis at 1.36 and 1.71 eV, respectively. A spin-split band gap has been proposed to explain the parallel observation of two absorption edges in ferromagnetic $Bi_2Fe_4O_9$ [6,33], and DFT calculations support this proposal, finding the density of states $N(E)$ at the bottom of the conduction band E_F to be mainly composed of nearly dispersionless states of predominantly octahedrally coordinated Fe-$3d$ character [34,35]. Although a number of magnetic origins have been put forth for the lower energy absorption edge observed in $Bi_2Fe_4O_9$, we caution that its nature remains controversial [36]. Nonetheless, the similarity suggests that $N(E)$ in $Bi_2CrAl_3O_9$ may likewise consist of largely Cr-$3d$ character near E_F and moreover that spin polarization may remain a feature of the electronic structure even at $T = 301$ K, the temperature at which our spectrum was collected. DFT calculations that we discuss below will clarify the nature of the states near the gap in $Bi_2CrAl_3O_9$. In any case, to place the magnitude of our observed gap in context, its extent is only half that of the 2.8 eV gap of undoped $Bi_2Al_4O_9$ [32]. Interestingly, it is also substantially narrower than the 2.1 eV gap of $Bi_2Fe_4O_9$ [37], suggesting that $Bi_2CrAl_3O_9$ is a comparatively more itinerant system.

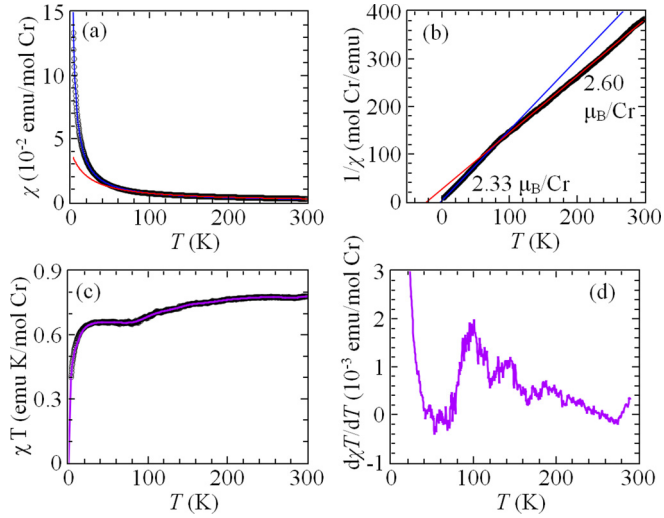

FIG. 3. (a) The temperature T dependence of the dc magnetic susceptibility $\chi = M/H$ with applied field $H = 10\,000$ Oe of a collection of $Bi_2CrAl_3O_9$ single crystals (black circles). Solid lines are fits as described in (b). (b) The T dependence of $1/\chi$ (black circles). The red and blue solid lines are fits to the Curie-Weiss law across temperature ranges $T > 80$ K and $T < 75$ K, respectively, and correspond to fluctuating moments of 2.60 ± 0.01 μ_B/Cr and 2.33 ± 0.01 μ_B/Cr, as indicated. (c) χT plotted as a function of T (black circles), clarifying the discontinuity in slope at 79 ± 3 K. The solid violet line is a smoothed representation of the data, obtained by 5 point moving window average. (d) The T dependence of Fisher's specific heat $d(\chi T)/dT$ computed from the smoothed curve in (d).

C. Magnetic fluctuations, order, and disorder

Figure 3 shows that $Bi_2CrAl_3O_9$ is a Curie-Weiss paramagnet above temperature $T^\star = 98 \pm 3$ K and suggests that this compound may enter an ordered or spin glass state with zero net magnetization M at this temperature. In Fig. 3(a), we plot the T dependence of the dc magnetic susceptibility $\chi = M/H$, where the field $H = 10,000$ Oe. As T is raised from 3.0 K, χ decreases sharply and monotonically, as expected by the Curie-Weiss law $\chi(T) = C/(T - \Theta_W)$, for Curie constant C and Weiss temperature Θ_W. The small magnitude of $\chi = 0.26 \times 10^{-2}$ emu/mol Cr at $T = 300$ K suggests that the sum of any T-independent contributions to χ such as Pauli, Van Vleck, or core diamagnetic susceptibilities is small—as is typical of an insulator—and we find it unnecessary to subtract a constant χ_0 from the presented data in subsequent analyses. The dominant contribution to χ is apparently Curie-Weiss-like in character, consistent with the presence of large and fluctuating Cr^{3+} local moments.

Closer inspection of the reciprocal susceptibility $1/\chi$ reveals a discontinuity in slope at 79 ± 3 K, as shown in Fig. 3(b). Within the range 80–300 K, the data are well modeled by a fluctuating moment corresponding to 2.60 ± 0.01 μ_B/Cr with a modest negative Weiss temperature $\Theta_W = -21 \pm 1$ K, indicating the local paramagnetic moments maintain a weak tendency towards antialignment. Below 75 K, the discontinuity in the slope of $1/\chi$ results in a ∼10% smaller fluctuating moment 2.33 ± 0.01 μ_B/Cr with vanishingly small $\Theta_W = -1.3 \pm 1$ K. Both of of our obtained fluctuating moments are notably less than the expected 3.8 μ_B/Cr^{3+} free ion value, suggesting that hybridization of the Cr-$3d$ orbitals in this system is important to an extent not observed in $Bi_2Fe_4O_9$ [16], a second indication that $Bi_2CrAl_3O_9$ is comparatively more itinerant. Interestingly, Cr substitution in the doped Cairo system $Bi_4Cr_xFe_{5-x}O_{13}F$ appears to reduce the fluctuating moment in that compound from 5.4 μ_B/Fe for $x = 0$ [17] to 3.9 μ_B per transition metal for $x = 1$, an effect ascribed to increased transition metal hybridization with O [38], suggesting that the enhanced itineracy we infer may be associated with disorder induced by Cr substitution.

The disappearance of ∼10% of the moment from the Curie-Weiss susceptibility in $Bi_2CrAl_3O_9$ implies that some 0.27 μ_B/Cr enters a net $M = 0$ antiferromagnetic or spin glass phase, while the remaining 2.33 ± 0.01 μ_B/Cr remains fluctuating at temperatures below the transition. The signature of this putative transition is more obvious in Fig. 3(c), which plots the T dependence of the product χT and betrays an obvious discontinuity of slope near $T = 80$ K. Multiplying the quantities χ and T has the undesirable effect of magnifying the portion of the measurement with the lowest ratio of signal to noise, so we smoothed the data by applying a moving window average. As the figure shows, the moving average provides an excellent representation of the data for $T > 20$ K, which includes the region of interest, and permits us to calculate Fisher's heat capacity by $d(\chi T)/dT \propto C_m$ the magnetic contribution to the specific heat [39]. As we show in Fig. 3(d), the quantity $d(\chi T)/dT$ exhibits a sharp increase coincident with the $1/\chi$ slope discontinuity at 79 ± 3 K before

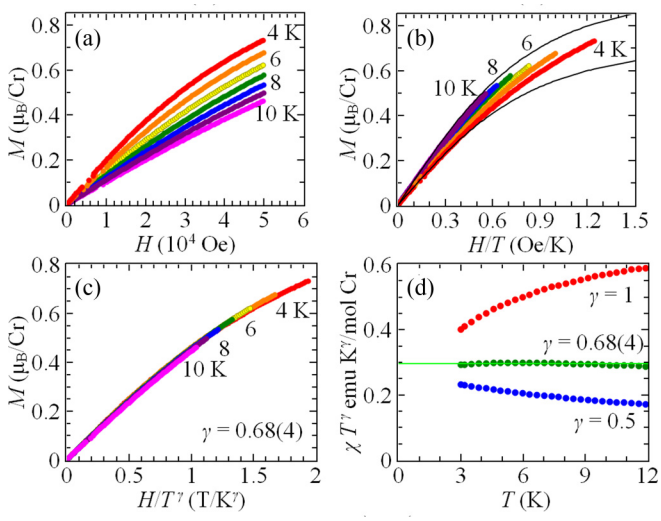

FIG. 4. (a) Magnetic isotherms measured with T incremented in 1 K steps as indicated. (b) Magnetization M plotted as a function of H/T to illustrate deviation from Brillouin functionlike behavior. Colors as in (a), as indicated. The upper and lower solid black lines are the $g = 2$, $J = 3/2$ Brillouin function with magnitude arbitrarily adjusted to the $T = 10$ and 4 K data, respectively. (c) M plotted as a function of H/T^γ with the critical exponent $\gamma = 0.68(4)$ indistinguishable from $\frac{2}{3}$, colors as in (a). (d) χT^γ plotted as a function of T for $\gamma = 1$ (red), 0.68(4) (green), and 0.5 (blue), with near T independence in the second case supporting the value of the critical exponent $\gamma = 0.68(4)$. The solid green line serves to provide a horizontal guide for the eye.

reaching a broad, pronounced maximum at $T^\star = 98 \pm 3$ K, which we identify as the transition temperature. Above this point, $d(\chi T)/dT$ decays slowly over a temperature range well in excess of 100 K, suggesting that short-range magnetic correlations remain significant at temperatures considerably beyond $T^\star$. We note that such a broad feature in C_m extending a factor of two or three above T_N is consistent with exact models of linear chains of finitely many Heisenberg moments with antiferromagnetic coupling [40], suggesting that similar physics may be at play here. Most interestingly, short-range antiferromagnetic order was very recently observed in neutron scattering experiments carried out above T_N in $Bi_2Fe_4O_9$, suggesting that the tenacity of short-range correlations beyond long-range ordering temperatures may be a general feature among magnetic $Bi_2M_4O_9$-type oxides [41].

We note that $T^\star$ is substantially greater than the magnitude of the Weiss temperature in the paramagnetic phase $\Theta_W = -21 \pm 1$ K. Given that Θ_W represents an average of the inter-moment coupling constants [42], this discrepancy implies that the statistical occupancy of the $Cr_{0.50}Al_{0.50}$ position gives rise to several local configurations with competing interactions, perhaps stemming from Cr chains of irregular lengths. That $\Theta_W < 0$ in bulk implies that the tendency towards anti-alignment is comparatively stronger, and it may be this interaction that gives rise to the presumptive phase transition at $T^\star = 98 \pm 3$ K involving ~10% of the fluctuating moment.

Figure 4 supports this picture of correlated, disordered chains and shows that M at $T \leqslant 10$ K cannot arise from individually fluctuating local moments. Plots of $M(H)$ displayed in Fig. 4(a) are nonlinear even at $T = 10$ K, and the nonlinearity becomes increasingly pronounced as T is lowered, appearing at first glance as would be expected of local paramagnetic moments. The observed $T \to 0$ moment at $H = 50\,000$ Oe approaches 0.8 μ_B/Cr, but remains short of saturation. When the same data are plotted as a function of H/T as in Fig. 4(b), however, the scaling is poor, and furthermore, they are clearly in discord with the Brillouin function B_J for $J = 3/2$ and $g = 2$, even if we constrain the overall magnitude of B_J for maximal agreement with the data. Plainly, the curvature of $M(H)$ is non-Brillouin-like, regardless of our choice of free parameters, leading us to conclude that the freely fluctuating moments of Fig. 3 develop correlations with their neighbors by $T \leqslant 10$ K.

Correspondingly, if we reject Brillouin H/T scaling, and instead plot M against H/T^γ, for critical exponent $\gamma = 0.68(4)$, the isotherms collapse to nearly a single curve as shown in Fig. 4(c). We note that achieving data collapse does not require implementation of a reduced temperature $t = T - T_c$ for some critical temperature T_c [43], suggesting that the fluctuations responsible for the observed scaling persist from an undetected transition that may occur at or near to $T_c = 0$ K. Moreover, that $\gamma < 1$ implies that these fluctuations may be associated with a disordered, potentially quasi-one-dimensional phase. By way of analogy, $\gamma < 1$ is found for the disordered phase of random transverse-field Ising spin chains (RTISC), which provide a convenient point of comparison in that they are exactly soluble across a wide range of parameters, including both ordered and disordered phases [44,45]. In disordered RTISC systems, χ diverges at low temperatures as $\chi(T) \sim 1/T^\gamma$ ($\gamma < 1$), suggesting that M adopts a universal function of H/T^γ for small H, just as we observe in $Bi_2CrAl_3O_9$ in Fig. 4(c). Meanwhile, plots of χT^γ shown in Fig. 4(d) clarify the concomitant $1/T^\gamma$-dependence of χ throughout this temperature range. As the figure shows, when $\gamma = 0.68(4)$, the quantity χT^γ is independent of T to within 1.4% across the range $3.0 \leqslant T \leqslant 12.0$ K, while the $\gamma = 1$ and $\gamma = 0.5$ curves betray obvious T dependence [also seen in Fig. 3(c) for $\gamma = 1$]. We do not mean to imply that $Bi_2CrAl_3O_9$ is necessarily an RTISC system, merely that the compositional disorder and low dimensionality that we infer from our crystallographic characterization of this system are potential roots of the observed H/T^γ scaling. We also reiterate that the sum χ_0 of any Pauli, Van Vleck, or core diamagnetic contributions is an $\mathcal{O}(1\%)$ effect. Accordingly, the observed $M(H/T^\gamma)$ arises solely from coexistence of a static moment associated with the $T^\star = 98 \pm 3$ K phase and thermal and quantum fluctuations of some ordered state, frustrated by chemical disorder, that would coalesce only at $T < 3$ K if at all.

D. Origin of the gap

Figure 5 shows the results of DFT calculations that reproduce the observed high-temperature gap and moment, while together emphasizing the importance of spin polarization at $T = 300$ K in $Bi_2CrAl_3O_9$. In the inset to Fig. 5(a), we show the assumed structure we used as the input for the calculations, which models the bulk, disordered $Cr_{0.5}Al_{0.5}$ site occupancy

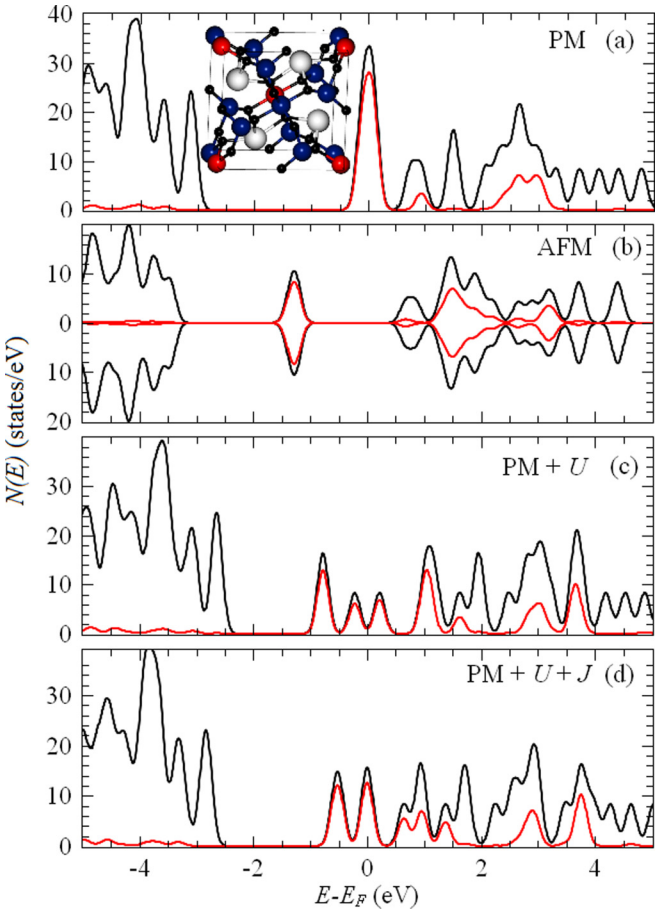

FIG. 5. (a) Density functional theory (DFT) calculation of the density of states $N(E)$ of $Bi_2CrAl_3O_9$ calculated in the absence of spin polarization (black line). The partial Cr-3d contribution to N is shown in red. (Inset) The input crystal structure of $Bi_2CrAl_3O_9$ that models the statistical occupancy of the $Cr_{0.5}Al_{0.5}$ sites for the calculations. Cr are colored in red, Al in blue, Bi in white, and O in black. (b) Spin polarized DFT calculations with an static antiferromagnetic moment corresponding to the experimental value, colors as in (a). (c) Nonspin polarized DFT calculations with Hubbard U calculated from first principles, colors as in (a). (c) Nonspin polarized DFT calculations with Hubbard U and Hund's J_H calculated from first principles, colors as in (a).

to first order by placing a Cr atom within every second octahedron. Calculations were performed with experimental lattice parameters and atomic positions. In contrast to $Bi_2Al_4O_9$, which is a simple band insulator [32], our calculations of the $N(E)$ within this model find a metallic ground state in nonspin polarized, uncorrelated (i.e., $U = 0$) $Bi_2CrAl_3O_9$. As we show in Fig. 5(a), the absence of spin polarization leaves minimally dispersive bands of predominantly Cr-3d character to dominate $N(E)$ near the Fermi energy E_F. The largest contribution to $N(E)$ in this range is a broad Cr-3d-derived peak. Clearly, the distorted octahedral crystal field we observe in our spectroscopic measurements is by itself far too weak to gap the Fermi surface. Of course, this supposed metallic DFT ground state is in direct contradiction with these very results. We conclude that the experimentally observed optical gap must therefore be opened by effects outside of DFT, such as U, spin-polarization, intra-atomic exchange, or some combination thereof.

We performed additional calculations to elucidate the mechanism responsible for opening the observed charge gap. Figure 5(b) shows DFT calculations performed under the assumption of a antiferromagnetic order with propagation vector $\mathbf{k} = (0, 0, 0)$ and static moment $\mu = 0.27\ \mu_B$/Cr as inferred from our magnetic measurements. With the addition of spin polarization to the model, a gap of 1.4 eV opens around $N(E)$, in excellent agreement with the observed experimental gap $\Delta E = 1.36$ eV, while we find a moment of 2.26 μ_B/Cr, again in strong accord with the $2.60 \pm 0.01\ \mu_B$/Cr experimental high-temperature paramagnetic moment. The sole addition of spin-polarization to this simplified DFT model removes these major, qualitative disparities with experiment.

While these calculations adequately model the observed properties in the presumptive ordered state below $T^\star = 98 \pm 3$ K, they do not explain why $Bi_2CrAl_3O_9$ remains insulating in the paramagnetic state. To address this discrepancy, we carried out DFT+U calculations in the absence of spin polarization, which we present in Fig. 5(c). Here, we apply a value of $U = 3.8$ eV, which we calculated from first principles according to a linear response technique [25]. As the figure shows, U prompts the formation of upper and lower Hubbard bands, but $N(E_F)$ remains finite at our realistic $U = 3.8$ eV. Even with the tendency of DFT to underestimate energy gaps, an eventual d-d Hubbard-type gap emerging from larger U would still remain well short of the wide 1.4 eV gap found in the spin-polarized calculations and the 1.36 eV gap observed in diffuse reflectance. We conclude that on-site Coulomb repulsion cannot alone be responsible for the observed optical gap above $T^\star$. Given the failure of realistic U to explain an observe charge gap beyond the onset of magnetic order [46], we determined a realistic Hund's $J_H = 0.9$ eV by an analogous technique. Interestingly, our DFT $+ U + J_H$ calculations in Fig. 5(d) show that the primary effect of J_H in this system is to merge the Hubbard bands. Typically, a charge gap is stabilized by J_H in systems with half-filled d orbitals, while itineracy is instead promoted in non-half-filled cases [47]. That J_H appears to promote metallicity in $Bi_2CrAl_3O_9$ suggests that the orbital hybridization we infer from magnetic measurements may marginally displace this material from the ideal half-filled 3d configuration. Given the inability of both U and $U + J_H$ calculations to achieve realistic gaps in this system, we are left to conclude that the dominant factor contributing to the observed charge gap above $T^\star$ is remnant spin polarization. This interpretation is consistent with our experimental observation of enhanced $d(\chi T)/dT$ even at temperatures well beyond the putative ordering temperature.

While our DFT calculations and magnetic measurements together point to an insulating state stabilized by wave vector-independent magnetic correlations, we cannot at this point rule out the possibility that the gap originates with a high-temperature charge density wave CDW or spin density wave SDW state. Specifically, at some temperature above 300 K, the quasi-one dimensional character of the crystal structure might result in electron-phonon interaction-induced distortion of the lattice and a gap opening in the Fermi surface at the nesting wave vector. Given the absence of evidence of such a phenomenon in our x-ray diffraction measurements,

the magnitude of any charge modulation would have to be small, perhaps only a few percent—for instance, as has been observed in transition metal chalcogenides [48]—and the resulting satellite peaks might be so weak as to be unambiguously detectable only through electron diffraction or synchrotron-based techniques. Conceivably, this purported distortion could explain the two-gap feature we observe in our spectroscopic measurements, as our diffuse reflectance technique integrates the gap over wave vectors. A hypothetical picture arises that a CDW transition that occurs at $T > 300\,K$ would open a second gap mostly at the nesting wave vector, which would modulate the gap generated primarily by local interactions. Further measurements, perhaps supported by more sophisticated dynamical mean field theory calculations, are required to confirm or to disprove this picture and to comment conclusively on the mechanism by which the gap is opened.

IV. CONCLUSIONS

Taken together, our experimental and theoretical results reveal that $Bi_2CrAl_3O_9$ is a magnetic insulator, in which the Cr^{3+} t_{2g}^3 $^4A_2$ ground state is stabilized by a distorted local octahedral symmetry, with the first excited ^2E doublet promoted some $\Delta E = 1.75$ eV above. The resulting high-spin t_{2g}^3 bands are subject to significant Cr-O hybridization and accordingly host local magnetic moments of $2.60 \pm 0.01\ \mu_B$/Cr, arranged in disordered chains and reduced in magnitude from the free ion value. At high temperatures, the dominant excitations of this configuration would be the spinons, and presumably they are gapped, permitting us to observe only the Curie-Weiss susceptibility of the moments themselves [49]. Meanwhile, short-range correlations remnant from the eventual ordered state perpetuate an insulating gap of width 1.36 eV even at temperatures well in excess of $T^\star = 98 \pm 3$ K. Below $T^\star$, a fraction of the overall moment coalesces into short-range order as the chains lock together, but this transition would only affect the lowest energy part of the spinon spectrum, and most of the spectral weight at higher energies is untouched by the onset of order. At the lowest temperatures, the static moment of the ordered state coexists with frustration-induced fluctuations among the disordered, correlated chains. If crystal sizes can be improved, inelastic neutron scattering measurements to probe the magnetic excitation spectrum would prove enlightening across these three distinct temperature regimes.

The structural framework from which these properties arise is a quasi-one dimensional chain of distorted, edge-sharing octahedra that x-ray diffraction measurements find to be occupied statistically by both Al and Cr^{3+}. This occupancy marks the single greatest structural difference between $Bi_2CrAl_3O_9$ and the Cairo pentagonal lattice compounds: Cr^{3+} is resident only within the octahedrally coordinated sites along these chains, while the interconnecting tetrahedra are relegated to the nonmagnetic Al species. Yet even with one of the two magnetic sites of $Bi_2Fe_4O_9$ essentially eliminated, while the remaining site is half-emptied and disordered, it is remarkable to what extent the emergent properties are qualitatively parallel between these two materials. Both host reasonably large, high-spin local moments, dual absorption edges within an insulating gap, and short-ranged correlations that stabilize this gap well into the paramagnetic phase. As some of the few realizations of the Cairo pentagonal lattice, $Bi_2Fe_4O_9$-like systems may have access to a rich and tunable collection of often exotic phases [12–14], but our study suggests that the local physics that ties together $Bi_2CrAl_3O_9$ and $Bi_2Fe_4O_9$ appears to be indelible.

This immutability suggests that the exotic states predicted to arise in Cairo pentagonal systems in the $J = 1/2$ quantum limit may prove to be inaccessible from the $Bi_2M_4O_9$ crystal structure across the range of transition metals $M = V^{3+} \cdots Ni^{3+}$ due to the challenge of realizing a $J = 1/2$ configuration. Our review of crystallographic databases finds that Cu does not appear to occupy the $Bi_2M_4O_9$ or related structure types in either its Cu^{1+} or Cu^{2+} configuration. It remains to be seen if Ti^{3+} ions—where $J = 1/2$ may be more feasible—will be sufficiently small as to fit in the tetrahedrally coordinated environment, occupancy that ultimately is required if the pentagonal lattice is to be completely filled. Like Cr^{3+}, Ti^{3+} appears to show limited solubility in $Bi_2M_4O_9$-type materials [50], and competing phases such as $Bi_2Ti_4O_{11}$ limit Ti occupancy to octahedrally coordinated sites, and even then, elementary valence counting suggests the nonmagnetic Ti^{4+} configuration to be preferred [51]. Realization in a $Bi_2Fe_4O_9$-like material of the predicted exotic quantum phases of Cairo systems might prove unattainable, requiring in the end the discovery of an entirely new crystal structure capable of hosting a pentagonal lattice.

ACKNOWLEDGMENTS

Acknowledgment is made to the Donors of the American Chemical Society Petroleum Research Fund, for support of this research under contract 56764-UNI10. The Stony Brook University single crystal diffractometer was obtained through the support of the National Science Foundation grant CHE-0840483. L.S. and M.C.A. were supported by NSF-DMR-13100008. J.C.U. was supported by an NYSED CSTEP Grant, under Contract No. C401633. J.W.S. was supported in part by a Provost's Research Fellowship from Farmingdale State College.

[1] M. Curti, A. Kirsch, L. I. Granone, F. Tarasi, G. López-Robledo, D. W. Bahnemann, M. M. Murshed, T. M. Gesing, and C. B. Mendive, ACS Catal. **8**, 8844 (2018).

[2] M. Back, J. Ueda, M. G. Brik, T. Lesniewski, M. Grinberg, and S. Tanabe, ACS Appl. Mater. Intervaces **10**, 41512 (2018).

[3] D. Chen, X. Chen, X. Li, H. Guo, S. Liu, and X. Li, Opt. Lett. **42**, 4950 (2017).

[4] M. Back, E. Trave, J. Ueda, and S. Tanabe, Chem. Mater. **28**, 8347 (2016).

[5] C. Liu, Z. Xia, M. Chen, M. S. Molokeev, and Q. Liu, Inorg. Chem. **54**, 1876 (2015).

[6] Y. Li, Y. Zhang, W. Ye, J. Yu, C. Lu, and L. Xia, New J. Chem. **36**, 1297 (2012).

[7] M. Pooladi, H. Shokrollahi, S. A. N. H. Lavasani, and H. Yang, Mater. Chem. Phys. **229**, 39 (2019).

[8] H. Shen, D. Yang, X. Lu, F. Mei, M. Zhou, X. Xu, X. Ren, F. Huang, and J. Zhu, J. Phys. D Appl. Phys. **51**, 295002 (2018).

[9] S. R. Mohapatra, B. Sahu, M. Chandresekhar, P. Kumar, S. D. Kaushik, S. Rath, and A. K. Singh, Ceram. Int. **42**, 12352 (2016).

[10] E. Ressouche, V. Simonet, B. Canals, M. Gospodinov, and V. Skumryev, Phys. Rev. Lett. **103**, 267204 (2009).

[11] F. C. Rodgrigues, S. M. de Souza, and O. Rojas, Ann. Phys. **379**, 1 (2017).

[12] I. Rousochatzakis, A. M. Läuchli, and R. Moessner, Phys. Rev. B **85**, 104415 (2012).

[13] A. Ralko, Phys. Rev. B **84**, 184434 (2011).

[14] M. Isoda, H. Nakano, and T. Sakai, J. Phys. Soc. Jpn. **83**, 084710 (2014).

[15] H. Nakano, M. Isoda, and T. Sakai, J. Phys. Soc. Jpn. **83**, 053702 (2014).

[16] N. Shamir, E. Gurewitz, and H. Shaked, Acta Cryst. A **34**, 662 (1978).

[17] A. M. Abakumov, D. Batuk, A. A. Tsirlin, C. Prescher, L. Dubrovinsky, D. V. Sheptyakov, W. Schnelle, J. Hadermann, and G. Van Tendeloo, Phys. Rev. B **87**, 024423 (2013).

[18] A. A. Tsirlin, I. Rousochatzakis, D. Filimonov, D. Batuk, M. Frontzek, and A. M. Abakumov, Phys. Rev. B **96**, 094420 (2017).

[19] V. Petříček, M. Dušek, and L. Palatinus, Z. Kristallogr. **229**, 345 (2014).

[20] L. Palatinus and G. Chapuis, J. Appl. Cryst. **40**, 786 (2007).

[21] K. Momma and F. Izumi, J. Appl. Crystallogr. **44**, 1272 (2011).

[22] P. Giannozzi, S. Baroni, N. Bonini, M. Calandra, R. Car, C. Cavazzoni, D. Ceresoli, G. L. Chiarotti, M. Cococcioni, I. Dabo, A. Dal Corso, S. Fabris, G. Fratesi, S. de Gironcoli, R. Gebauer, U. Gerstmann, C. Gougoussis, A. Kokalj, M. Lazzeri, L. Martin-Samos, N. Marzari, F. Mauri, R. Mazzarello, S. Paolini, A. Pasquarello, L. Paulatto, C. Sbraccia, S. Scandolo, G. Sclauzero, A. P. Seitsonen, A. Smogunov, P. Umari, and R. M. Wentzcovitch, J. Phys.: Condens. Matter **21**, 395502 (2009).

[23] P. Giannozzi, O. Andreussi, T. Brumme, O. Bunau, M. Buongiorno Nardelli, M. Calandra, R. Car, C. Cavazzoni, D. Ceresoli, M. Cococcioni, N. Colonna, I. Carnimeo, A. Dal Corso, S. de Gironcoli, P. Delugas, R. A. DiStasio, Jr., A. Ferretti, A. Floris, G. Fratesi, G. Fugallo, R. Gebauer, U. Gerstmann, F. Giustino, T. Gorni, J. Jia, M. Kawamura, H.-Y. Ko, A. Kokalj, E. Küçükbenli, M. Lazzeri, M. Marsili, N. Marzari, F. Mauri, N. L. Nguyen, H.-V. Nguyen, A. Otero-de-la-Roza, L. Paulatto, S. Poncé, D. Rocca, R. Sabatini, B. Santra, M. Schlipf, A. P. Seitsonen, A. Smogunov, I. Timrov, T. Thonhauser, P. Umari, N. Vast, X. Wu, and S. Baroni, J. Phys.: Condens. Matter **29**, 465901 (2017).

[24] G. Prandini, A. Marrazzo, I. E. Castelli, N. Mounet, and N. Marzari, NPJ Comput. Mater. **4**, 72 (2018).

[25] M. Cococcioni and S. de Gironcoli, Phys. Rev. B **71**, 035105 (2005).

[26] B. Himmetoglu, R. M. Wentzcovitch, and M. Cococcioni, Phys. Rev. B **84**, 115108 (2011).

[27] T. Debnath, A. Ullah, C. H. Rüscher, and A. Hussain, J. Solid State. Chem. **220**, 167 (2014).

[28] D. M. Giaquinta, G. C. Papaefthymiou, and H.-C. zur Loye, J. Sol. State. Chem. **114**, 199 (1995).

[29] D. L. Wood, J. Ferguson, K. Knox, and J. F. Dillon, Jr., J. Chem. Phys. **39**, 890 (1963).

[30] S. Sugano, Y. Tanabe, and H. Kamimura, *Multiplets of Transition-Metal Ions in Crystals* (Academic Press, New York, 1970).

[31] M. D. Sturge, H. J. Guggenheim, and M. H. L. Pryce, Phys. Rev. B **2**, 2459 (1970).

[32] E. Zahedi, B. Xiao, and M. Shayestefar, Inorg. Chem. **55**, 4824 (2016).

[33] S. Sun, W. Wang, L. Zhang, and M. Shang, J. Phys. Chem. C **113**, 12826 (2009).

[34] Z. V. Pchelkina and S. V. Streltsov, Phys. Rev. B **88**, 054424 (2013).

[35] Y. Zhang, Y. Guo, H. Duan, H. Li, L. Yang, P. Wang, C. Sun, B. Xu, and H. Liu, RSC Adv. **4**, 28209 (2014).

[36] For a discussion, see: A. Kirsch, M. M. Murshed, M. Schowalter, A. Rosenauer, and T. M. Gesing, J. Phys. Chem. C **120**, 18831 (2016) and references therein.

[37] A. Kirsch, M. M. Murshed, F. J. Litterst, and T. M. Gesing, J. Phys. Chem. C **123**, 3161 (2019).

[38] M. G. Rozova, V. V. Grigoriev, O. A. Tyablikov, D. S. Filimonov, K. V. Zakharov, O. S. Volkova, A. N. Vasliev, E. V. Antopov, and A. M. Abakumov, Mater. Res. Bull. **87**, 54 (2017).

[39] M. E. Fisher, Phil. Mag. **7**, 1731 (1962).

[40] J. C. Bonner and M. E. Fisher, Phys. Rev. **135**, A640 (1964).

[41] A. K. Singh, S. R. Mohapatra, P. Khare, N. Ganguli, A. Wildes, V. Siruguri, and S. D. Kaushki, Mater. Res. Express **6**, 066107 (2019).

[42] A. Czachor, J. Magn. Magn. Mater. **139**, 355 (1995).

[43] J. Zinn-Justin, *Quantum Field Theory and Critical Phenomena* (Clarendon, Oxford, 1996), 3rd. ed.

[44] D. S. Fisher, Phys. Rev. B **51**, 6411 (1995).

[45] F. Iglói and C. Monthus, Phys. Rep. **412**, 277 (2005).

[46] D. E. McNally, J. W. Simonson, K. W. Post, Z. P. Yin, M. Pezzoli, G. J. Smith, V. Leyva, C. Marques, L. DeBeer-Schmitt, A. I. Kolesnikov, Y. Zhao, J. W. Lynn, D. N. Basov, G. Kotliar, and M. C. Aronson, Phys. Rev. B **90**, 180403(R) (2014).

[47] L. de' Medici, J. Mravlje, and A. Georges, Phys. Rev. Lett. **107**, 256401 (2011).

[48] E. DiMasi, B. Foran, M. C. Aronson, and S. Lee, Phys. Rev. B **54**, 13587 (1996).

[49] W. J. Gannon, I. A. Zaliznyak, L. S. Wu, A. E. Feiguin, A. M. Tsvelik, F. Demmel, Y. Qiu, J. R. D. Copley, M. S. Kim, and M. C. Aronson, Nat. Commun. **10**, 1123 (2019).

[50] M. Krzhizhanovskaya, S. Filatov, V. Gusarov, P. Paufler, R. Bubnova, M. Morozov, and D. C. Meyer, Z. Anorg. Chem. **631**, 1603 (2005).

[51] V. Kahlenberg and H. Böhm, Acta Cryst. **B51**, 11 (1995).